The Astrophysical Journal, 997:220 (7pp), 2026 February 1 https://doi.org/10.3847/1538-4357/ae27d3

Formation of the Energetic Electrons at the Dipolarization Front and the Trailing Flux Pileup Region during Magnetic Reconnection

Jia Nan[1,2], Quanming Lu[1,2], Kai Huang[3], San Lu[1,2], Rongsheng Wang[1,2], and Shihang Hu[1,2]
[1] School of Earth and Space Sciences/Deep Space Exploration Laboratory, University of Science and Technology of China, Hefei 230026, People's Republic of China; qmlu@ustc.edu.cn
[2] Collaborative Innovation Center of Astronautical Science and Technology, Harbin, People's Republic of China
[3] School of Physics, Harbin Institute of Technology, Harbin 150001, People's Republic of China; khuang@hit.edu.cn
Received 2025 October 30; revised 2025 November 28; accepted 2025 December 2; published 2026 January 23

Abstract

The dipolarization front (DF) and the flux pileup region (FPR) are crucial downstream structures in magnetic reconnection, where significant energetic electrons are frequently observed. Using a two-dimensional particle-in-cell simulation model, we investigate the formation of energetic electrons in both the DF and the trailing FPR. Our results demonstrate that the energetic electrons at pitch angles near 90° at both regions undergo a two-stage acceleration process: an initial nonadiabatic acceleration by the reconnection electric field at the reconnection site followed by downstream adiabatic acceleration. We find that the 90° pitch-angle energetic electrons in the FPR reach substantially higher energies than those at the DF, since they encounter a stronger reconnection electric field at the reconnection site in the first stage. Furthermore, two populations of energetic electrons with distinct energy ranges at pitch angles near 0° and 180° are identified at the DF. The lower-energy population exhibits energies close to the magnitude of the parallel potential at the DF, which dominates the formation of this population by accelerating the electrons towards the DF and providing the trapping mechanism. The higher-energy population is energized via the Fermi mechanism through multiple reflections within the contracting magnetic island downstream. These findings provide new insights into the generation of energetic electrons during magnetic reconnection.

Unified Astronomy Thesaurus concepts: Space plasmas (1544); Plasma physics (2089); Planetary magnetospheres (997)

1. Introduction

Magnetic reconnection is a fundamental physical process in plasma for energy conversion from magnetic energy into particle kinetic energy, and it drives explosive phenomena in space, astrophysical, and laboratory plasmas (R. Giovanelli 1946; P. Sweet 1958; A. Nishida & S.-I. Akasofu 1979; R. McPherron 1987; S. Tsuneta et al. 1992; J. Lin & T. Forbes 2000; V. Angelopoulos et al. 2008; M. Yamada et al. 2010; T. Zhang et al. 2012; Y.-H. Liu et al. 2017; Y. Shu et al. 2021; Q. Lu et al. 2022, 2025; R. Wang et al. 2023; L. Dai et al. 2024; S. Wang et al. 2024; K. Huang et al. 2025a, 2025b; F. Yang et al. 2025). Magnetic reconnection features a multiscale diffusion region characterized by a small electron diffusion region (EDR) embedded within a more extensive ion diffusion region (IDR; J. Birn & M. Hesse 2001; P. Pritchett 2001; F. Mozer et al. 2002; T. Nagai et al. 2003; Q. Lu et al. 2010; A. Divin et al. 2012). Furthermore, magnetic reconnection generates crucial downstream signatures, including the flux pileup region (FPR; M. Hesse & J. Birn 1991; H. Zhang et al. 2007; M. Wu et al. 2015; C. Liu et al. 2017) and dipolarization front (DF; V. Angelopoulos et al. 1992; M. Ashour-Abdalla et al. 2011; H. Fu et al. 2013; S. Lu et al. 2015, 2016).

The FPR forms where magnetic flux accumulates as a high-speed reconnection outflow decelerates upon colliding with the pre-existing plasma sheet (M. Hoshino et al. 2001; C. Liu et al. 2020). The leading edge of this propagating structure is known as the DF, characterized by a sharp increase in the magnetic field component normal to the neutral sheet (M. Sitnov et al. 2009; M. Wu et al. 2013; Y. Shu et al. 2021; M. Oka et al. 2023), which is also called the reconnection front. The DFs and their trailing FPRs are frequently detected by in situ spacecraft measurements in the Earth's magnetotail plasma sheet (R. Nakamura et al. 2002; A. Runov et al. 2009; M. Sitnov et al. 2009; M. Wu et al. 2013; C. Liu et al. 2017), and the significant enhancements in energetic electron flux are observed within these regions (V. Angelopoulos et al. 2013; M. Zhou et al. 2013; J. Birn et al. 2014; S. Huang et al. 2015; H. Fu et al. 2019; X. Xing et al. 2024).

The generation mechanism of energetic electrons at the DF and FPR has drawn significant attention in recent years. Within these structures, electrons can gain perpendicular energy through betatron acceleration, as they encounter the enhanced magnetic field of the piling magnetic flux (H. S. Fu et al. 2011; J. Birn et al. 2013; C. Huang et al. 2015; K. Huang et al. 2021; Y. Yu et al. 2023). They can also undergo Fermi acceleration, gaining parallel energy through repeated reflections along contracting magnetic field lines in the outflow region (J. Drake et al. 2006; X. R. Fu et al. 2006; S. Lu et al. 2016; C. Liu et al. 2017; Q. Lu et al. 2018; K. Huang et al. 2021). The parallel electric field is also found to be important to provide the trapping mechanism, enabling continuous and efficient betatron acceleration at the DF (C. Huang et al. 2015). In addition to these downstream processes, the electron acceleration at the reconnection site (near the X-line) is another vital process for the generation of energetic electrons, as evidenced by numerous simulations and in situ observations (M. Øieroset et al. 2002; X. R. Fu et al. 2006; R. Wang et al. 2010a, 2010b;

C. Huang et al. 2010; S. Huang et al. 2012). The existence of these distinct acceleration processes suggests that electrons may go through a multistage acceleration process. M. Hoshino et al. (2001) proposed that electrons are primarily accelerated by the reconnection electric field near the X-line, and subsequently undergo further energization via gradient and curvature drift motion within the FPR. Observational works in the Earth's magnetotail also suggest that electrons can experience a multistage acceleration process (M. Wu et al. 2015; Y. Xu et al. 2018). Meanwhile, energetic electrons with diverse pitch-angle distributions are frequently observed at the DF and FPR (H. S. Fu et al. 2011; M. Wu et al. 2013; C. Liu et al. 2017). However, the specific connection between the different energization processes and the role of those processes in the formation of energetic electrons at different pitch angles observed at the DF/FPR remain unclear.

In this work, by utilizing a two-dimensional particle-in-cell (PIC) simulation, we study the formation of energetic electrons in the DF and its trailing FPR during magnetic reconnection. In our results, the energetic electrons in the FPR are predominantly concentrated at pitch angles near 90°, whereas those at the DF are observed at pitch angles near 0°, 90°, and 180°. We find that the 90° pitch-angle energetic electrons in both regions undergo a two-stage acceleration process, in which electrons are initially accelerated at the reconnection site by the reconnection electric field and are then transported downstream where they undergo further adiabatic acceleration. Furthermore, we identify two populations of energetic electrons with distinct energy ranges at pitch angles near 0° and 180°, and demonstrate their different formation mechanisms.

2. Simulation Model

This study is conducted by performing a two-dimensional PIC simulation. The software used in this paper has been successfully validated in our previous works on magnetic reconnection and plasma waves (X. R. Fu et al. 2006; Q. Lu et al. 2010; C. Chang et al. 2021; J. Nan et al. 2022). The simulation domain is in the x-z plane. A Harris current sheet with no guide field is given as the initial configuration:

$$\boldsymbol{B} = B_0 \tanh(z/\delta)\mathbf{e_x}, \quad (1)$$

$$n = n_0 \mathrm{sech}^2(z/\delta) + n_b, \quad (2)$$

where B_0 represents the asymptotic magnitude of the magnetic field, δ represents the half-thickness of the current sheet, and n_0 and n_b represent the peak density of current sheet and the background density, respectively. Here, we use $n_b = 0.05n_0$ and $\delta = 0.75d_i$, where d_i is the ion inertial length based on n_0. Two plasma species, electrons and ions, are used in the simulation. The reduced mass ratio is set to be $m_i/m_e = 100$. The initial velocity distributions of the two species are Maxwellian with temperature ratio $T_i/T_e = 4$, and the temperature of the current sheet plasma is 4 times that of the background plasma. The speed of light is set to be $c/V_A = 15$, where $V_A = B_0/\sqrt{n_0 m_i \mu_0}$ is the Alfvén speed, and the upstream Alfvén speed is defined as $V_{Ab} = B_0/\sqrt{n_b m_i \mu_0}$ based on background plasma density.

The simulation box is $L_x \times L_z = 100d_i \times 40d_i$. The spatial resolution is $\Delta x = \Delta z = 0.025d_i$. The time step adopted to push the simulation forward is $\Delta t = 0.001\Omega_i^{-1}$, where $\Omega_i = eB_0/m_i$ is the ion gyrofrequency. In the z direction, perfect conducting boundaries are used for electromagnetic field and reflecting boundaries are used for particles. Periodic boundaries are used in the x direction. A total of 1×10^9 pseudoparticles of each species are used in the simulation. In order to trigger the reconnection, we impose an initial perturbation of magnetic flux on the equilibrium state in the form of $\psi_1 = 0.1\, B_0\, d_i\, \mathrm{sech}^2\,(x/2\delta)\, \mathrm{sech}^2\,(z/\delta)$.

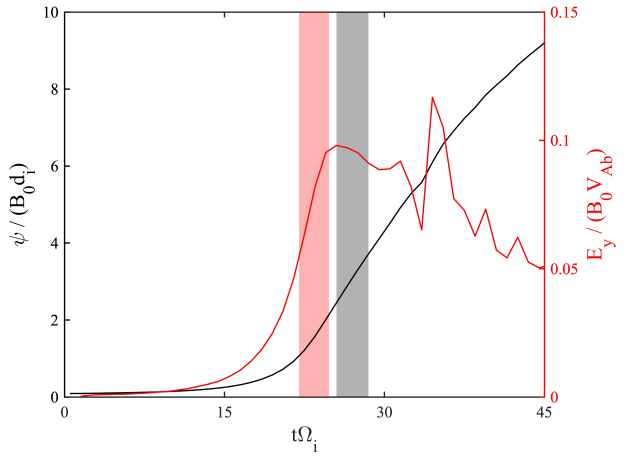

Figure 1. Time evolution of the magnetic flux ψ (black line) and the reconnection electric field E_y (red line) at the X-line. The red and gray shaded regions represent the time intervals $t\Omega_i = 22$–24.8 and $t\Omega_i = 25.5$–28.5, during which the retraced electrons originating from the DF and FPR (denoted in the white solid boxes in Figures 3(b1)–(b2)) travel through the reconnection site, correspondingly.

3. Results

Figure 1 shows the evolution of the magnetic flux ψ and the reconnection electric field E_y at the X-line. The magnetic reconnection starts quickly at approximately $t\Omega_i = 15$ under the trigger of the imposed initial perturbation. The reconnection electric field E_y at the X-line reaches its first peak of about $0.1B_0V_{Ab}$ at around $t\Omega_i = 25.5$, which is consistent with previous results (Y.-H. Liu et al. 2017; J. Nan et al. 2022; Q. Lu et al. 2025). Subsequently, the reconnection electric field decays slowly, although there are some fluctuations, and drops to about $0.05B_0V_{Ab}$ at $t\Omega_i = 45$.

Figure 2 displays the spatial distributions of (a1)–(a2) the magnetic field magnitude B, (b1)–(b2) the parallel potential $e\phi_\parallel$, (c1)–(c2) the electron perpendicular temperature $T_{e\perp}$, (d1)–(d2) the electron parallel temperature $T_{e\parallel}$, and (e1)–(e2) the temperature ratio $T_{e\perp}/T_{e\parallel}$ at $t\Omega_i = 32$ and 40, respectively. The definition of the parallel potential is $e\phi_\parallel(x, z) = e\int_{(x,z)}^{\infty} E_\parallel dl$, the integration of the work done by the parallel electric field on electrons along the magnetic field lines (J. Egedal et al. 2015; J. Nan et al. 2022). The two time slots are selected to describe the development of the DF and FPR. We identify the DF as the region centered around the magnetic field maximum along the $z = 0$ and spanning approximately one ion inertial length ($\sim 1\, d_i$) in extent. The trailing region of the DF is the FPR, which is distinguished as the region where $(\partial B/\partial t + V_{\mathrm{flux},x}\partial B/\partial x) > 0$ is satisfied in the downstream of the EDR, where $V_{\mathrm{flux},x}$ is the propagation speed of the magnetic flux in the x direction calculated by tracing the same magnetic flux along the $z = 0$. The DF and FPR ranges along the $z = 0$ are shown in Figures 2(f1)–(f2). At $t\Omega_i = 32$, the early stage of the DF, these two regions exhibit distinct plasma

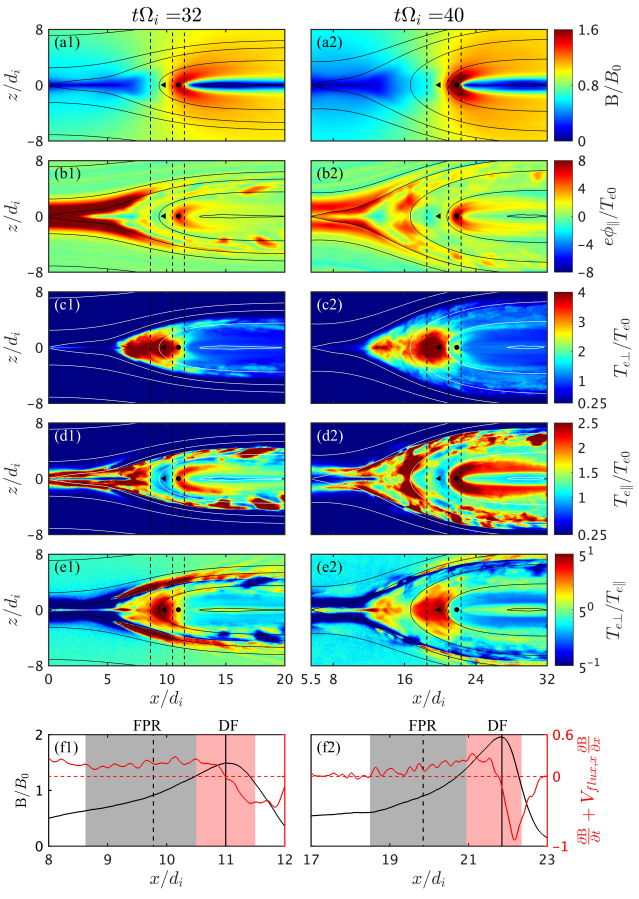

Figure 2. (a1)–(a2) The magnitude of magnetic field B, (b1)–(b2) the parallel potential $e\phi_\parallel$, where we define $e\phi_\parallel(x, z) = e\int_{(x,z)}^{\infty} E_\parallel dl$, the integration of the work done by parallel electric field on electrons from the boundary along the magnetic field lines, (c1)–(c2) the electron perpendicular temperature $T_{e\perp}$, (d1)–(d2) the electron parallel temperature $T_{e\parallel}$, and (e1)–(e2) the temperature ratio $T_{e\perp}/T_{e\parallel}$ at $t\Omega_i = 32$ and 40, respectively. The curves represent the magnetic field lines. Three vertical lines denote the boundaries separating the FPR (left) and the DF (right). (f1)–(f2) ($\frac{\partial B}{\partial t} + V_{\mathrm{flux},x}\frac{\partial B}{\partial x}$) (red lines) and the magnetic field magnitude (black lines) along $z = 0$ plane at $t\Omega_i = 32$ and 40, where $V_{\mathrm{flux},x}$ is the propagation speed of the magnetic flux in the x direction. The shaded regions represent the FPR (gray) and DF (red). Note that the left boundary of the FPR at $t\Omega_i = 32$ is determined by the EDR boundary. Representative locations at the DF and FPR are marked correspondingly by filled triangles and rounds in panels (a1)–(e1) and (a2)–(e2), and vertical lines in panels (f1)–(f2).

and field characteristics. The magnetic field strength is significantly enhanced at the DF, reaching approximately 1.5 B_0, while it is comparatively weaker in the trailing FPR. A strong, localized parallel potential($e\phi_\parallel$) with a magnitude up to $6T_{e0}$ (equivalent to $24T_{eb}$) develops at the DF, primarily resulting from the charge separation, which has already been studied in previous works (C. Huang et al. 2015; S. Hu et al. 2025). However, the parallel potential in the FPR is substantially weaker. Although both regions show significant perpendicular heating, the average perpendicular temperature in the FPR (about $5T_{e0}$) is notably higher than at the DF(about $3T_{e0}$). Conversely, the DF exhibits enhanced parallel temperature, with $T_{e\parallel}$ reaching around $2T_{e0}$, whereas there is no obvious parallel heating in the FPR. This suggests that the DF possesses a parallel energization that is absent in the FPR. Consequently, a strong temperature anisotropy of $T_{e\perp}/T_{e\parallel} > 1$ is developed at the FPR, while the parallel and perpendicular

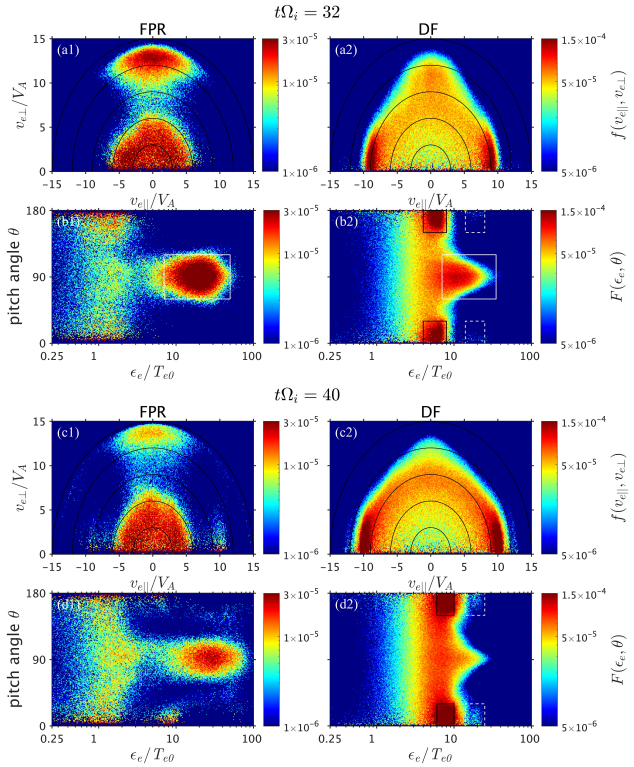

Figure 3. (a1)–(a2) and (c1)–(c2) the normalized velocity distribution of electrons $f(v_{e\parallel}, v_{e\perp})$, (b1)–(b2) and (d1)–(d2) the normalized energy spectrum at different pitch angles $F(\epsilon_e, \theta)$ at the selected locations of DF and FPR at $t\Omega_i = 32$ and 40 (as denoted in Figure 2), where ϵ_e represents electron energy and θ represents the pitch angle. Here $\iint f(v_{e\parallel}, v_{e\perp})v_{e\perp}dv_{e\perp}dv_{e\parallel} = \iint F(\epsilon_e, \theta)\sin(\theta)d\epsilon_e d\theta = n_e/n_0$, where n_e is the local electron density. The energetic electrons at pitch angles $|\theta - 90°| < 30°$ with energies $7T_{e0} < \epsilon_e < 50T_{e0}$ at the FPR and energies $7T_{e0} < \epsilon_e < 35T_{e0}$ at the DF are denoted by the white solid boxes in (b1)–(b2) at $t\Omega_i = 32$, respectively. The energetic electrons at pitch angles $|\theta - 90°| > 60°$ at the DF with energies $4T_{e0} < \epsilon_e < 8T_{e0}$ at $t\Omega_i = 32$ and energies $6T_{e0} < \epsilon_e < 10T_{e0}$ at $t\Omega_i = 40$ are denoted by black boxes in panel (b2) and panel (d2), respectively. The energetic electrons at pitch angles $|\theta - 90°| > 60°$ with energies $14T_{e0} < \epsilon_e < 25T_{e0}$ at the DF are denoted by white dashed boxes at the two time slots.

temperature are comparable at the DF at this time. At $t\Omega_i = 40$, the DF has evolved into a developed state, in which the magnetic field at the DF intensifies further to a magnitude of $2B_0$. Meanwhile, the parallel potential increases to approximately $8T_{e0}$. Concurrently, the DF exhibits increased parallel temperature (around $2.8T_{e0}$) alongside a decrease in the perpendicular temperature (around $2.2T_{e0}$). This leads to the development of a temperature anisotropy of $T_{e\perp}/T_{e\parallel} < 1$ at the DF, whereas the condition $T_{e\perp}/T_{e\parallel} > 1$ is maintained in the FPR. Representative locations in each region are selected and marked in Figure 2 for further analysis.

Figure 3 presents the normalized electron velocity distribution $f(v_{e\parallel}, v_{e\perp})$ and the normalized energy spectrum at different pitch angles $F(\epsilon_e, \theta)$ at representative locations within the FPR and DF at $t\Omega_i = 32$ and 40. The normalization adopted here is $\iint f(v_{e\parallel}, v_{e\perp})v_{e\perp}dv_{e\perp}dv_{e\parallel} = \iint F(\epsilon_e, \theta)\sin(\theta)d\epsilon_e d\theta = n_e/n_0$, where n_e is the local electron density. At $t\Omega_i = 32$, energetic electrons in the FPR (Figures 3(a1) and (b1)) are primarily concentrated at pitch angles near 90°. This population has an averaged energy of about $21T_{e0}$ with a maximum energy reaching up to about $70T_{e0}$ (denoted by the white solid box in

Figure 3(b1)). The remaining population in the FPR consists of a nearly isotropic, low-energy thermal component with energies below $3T_{e0}$. At the DF (Figures 3(a2) and (b2)), the energetic electrons are distributed at pitch angles near 0°, 90°, and 180°. The 90° pitch-angle population (denoted by the white solid box in Figure 3(b2)) has an average energy of about $12T_{e0}$ with a maximum energy up to approximately $40T_{e0}$, which is considerably lower than that in the FPR. Two populations of energetic electrons with distinct energy ranges are present at pitch angles near 0° and 180° at the DF. The lower-energy population consists of electrons with energies in the range of 4–$8T_{e0}$ (denoted by black boxes in Figure 3(b2)), close to the magnitude of the parallel potential at the DF($\sim 6T_{e0}$). It turns out that the parallel potential dominates the formation of this population, which will be displayed in detail later. The higher-energy population spans an energy range of about 14–$25T_{e0}$ (denoted by white dashed boxes in Figure 3(b2)), well exceeding the magnitude of the parallel potential. This population is attributed to the Fermi acceleration process (X. R. Fu et al. 2006; K. Huang et al. 2021), whereby electrons are energized through multiple reflections within the contracting magnetic island formed downstream due to periodic boundaries in the x direction.

We next examine the electron distributions at these two regions at $t\Omega_i = 40$, when the DF is well developed. In the FPR (Figures 3(c1) and (d1)), the electron distribution is still primarily composed of the 90° pitch-angle energetic population and the low-energy thermal population, similar to that at the earlier time. The energies of the high-energy population increase further, but the phase space density of this population is substantially reduced. At the DF (Figures 3(c2) and (d2)), a decrease in the energy spectrum of energetic electrons at pitch angles near 90° is observed. This is attributed to particle loss along the magnetic field, driven by the magnetic mirror force originating from the localized magnetic hump at the DF (K. Huang et al. 2021). Meanwhile, the energies of the lower-energy population at pitch angles near 0° and 180° are increased to 6–$10T_{e0}$(denoted by black solid boxes in Figure 3(d2)), corresponding to the intensification of the parallel potential to $\sim 8T_{e0}$. The energy spectrum of the higher-energy population at pitch angles near 0° and 180° is notably enhanced (denoted by white dashed boxes in Figure 3(d2)), consistent with K. Huang et al. (2021) that the contribution from Fermi reflection is more significant in later stage. We have confirmed that the formation of this higher-energy population is due to the Fermi process through particle tracing, but given that it has been detailed in the previous works (X. R. Fu et al. 2006; K. Huang et al. 2021), the analysis is not repeated here.

To understand the acceleration processes of energetic electrons observed at the DF and FPR, we retrace the trajectories (backward in time) of those electrons selected at $t\Omega_i = 32$, when the flux of 90° pitch-angle energetic electrons at the DF has not decreased. We first describe the formation of the 90° pitch-angle energetic populations at these two regions (denoted in white solid boxes in Figures 3(b1)–(b2)). Figure 4 shows the spatial distributions of the retraced electrons originating from the DF (a1)–(d1) and FPR (a2)–(d2) at different time slots. Figure 5 shows the time evolution of their averaged (a) magnetic moment μ, (b) electron energy ϵ_e, (c) local magnetic field magnitude B, and (d) $|\theta - 90°|$, where θ is the pitch angle. To simplify the description, we hereafter refer

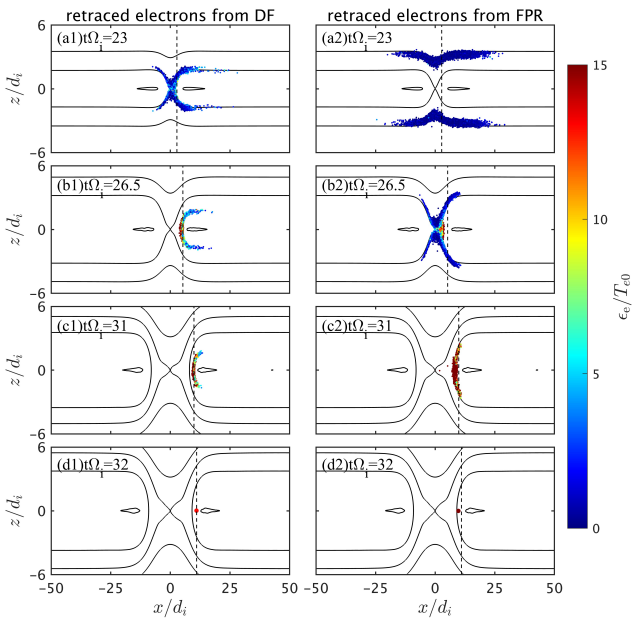

Figure 4. Spatial distributions for the retraced energetic electrons with pitch angles near 90°($|\theta - 90°| < 30°$) from (a1)–(d1) the DF and (a2)–(d2) FPR at $\Omega_i t$ = 23, 26, 31 and 32. Those retraced electrons are denoted in white solid boxes in Figures 3(b1) and 3(b2). The vertical dashed lines mark the location of the maximum of B along $z = 0$ in $x > 0$ domain at each time slot for reference. The colors represent the energies of electrons. The curves represent the magnetic field lines.

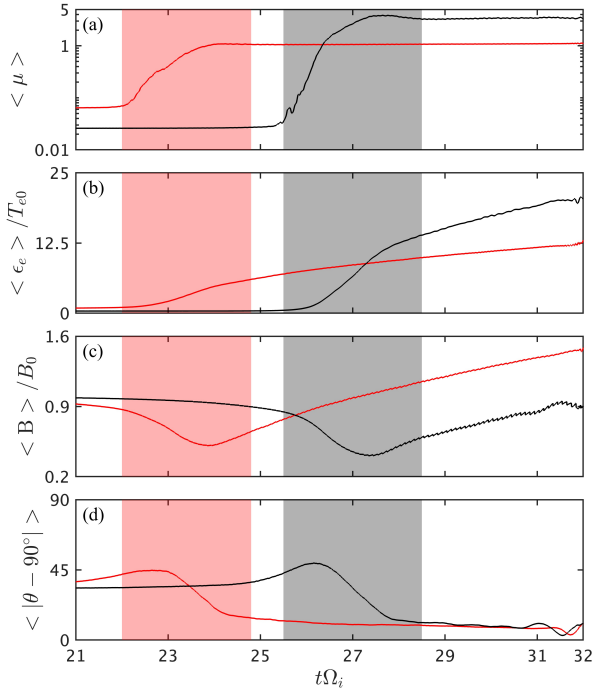

Figure 5. Time evolution of averaged (a) magnetic moment μ, (b) electron energy ϵ_e, (c) local magnetic field B, and (d) $|\theta - 90°|$, where θ is the pitch angle, of the retraced electrons with pitch angles near 90°($|\theta - 90°| < 30°$) from the DF (red lines) and FPR (black lines) at $t\Omega_i = 32$, respectively. The red and gray shaded regions mark the time intervals during which the averaged magnetic moment of the retraced electrons from the DF and FPR are not conserved, respectively.

to these populations as DF electrons and FPR electrons, respectively. Both the DF electrons and FPR electrons experience a two-stage acceleration process, which is an

initial nonadiabatic acceleration near the X-line, followed by an adiabatic acceleration in the outflow region. In the first stage, electrons are accelerated by reconnection electric field at the reconnection site, where their magnetic moment is not conserved. The DF electrons undergo this first-stage acceleration at about $t\Omega_i = 22$–24.8 (as shown in Figure 4(a1)), gaining an average energy of $5T_{e0}$ (red shaded region in Figure 5). In contrast, the FPR electrons pass through the reconnection site later around $t\Omega_i = 25.5$–28.5 (as shown in Figure 4(b2)), when the reconnection electric field is stronger than that experienced by the DF electrons (the time periods are also denoted in Figure 1), allowing FPR electrons to gain a higher energy of $13.4T_{e0}$ on average (gray shaded region in Figure 5). In the second stage, electrons are transported downstream and undergo an adiabatic acceleration due to the magnetic field compression with conserved magnetic moment. During this stage, the pitch angles of those electrons are very close to 90° (the averaged $|\theta - 90°|$ is less than 15° as shown in Figure 5(d)), which means that the energies of those electrons are mainly allocated in the perpendicular direction. Therefore, the energization efficiency of individual electrons can be described by

$$\frac{\mathrm{d}\epsilon_e}{\mathrm{d}t} = \mu\frac{\mathrm{d}B}{\mathrm{d}t} = \frac{\epsilon_{e0}}{B_0}\frac{\mathrm{d}B}{\mathrm{d}t}, \tag{3}$$

where ϵ_{e0} is the electron energy and B_0 is the local magnetic field strength at the beginning of this stage. Integrating Equation (3) yields $\epsilon_e = \epsilon_{e0}B/B_0$, which suggests that the final energy ϵ_e in the second stage depends on two factors: the initial energy ϵ_{e0} and the relative change in magnetic field (B/B_0). Although the DF electrons experience a larger magnetic field amplification ($B/B_0 = 2.26$ on average) compared to the FPR electrons ($B/B_0 = 1.52$ on average), their initial energies are significantly lower in this stage ($\epsilon_{e0} = 6.0T_{e0}$ for DF electrons and $\epsilon_{e0} = 13.9T_{e0}$ for FPR electrons on average). Ultimately, the electrons arriving at the FPR reach higher final energies ($20.7T_{e0}$ on average) compared with those arriving at the DF ($12.4T_{e0}$ on average).

A distinguishing feature of the energetic electron distribution at the DF is the presence of the lower-energy population at pitch angles near 0° and 180° (denoted by black solid boxes in Figure 3(b2)), which is absent in the FPR. The formation of this population can be categorized into three pathways, as illustrated by the spatial distributions of the retraced electrons in Figure 6. Figure 7 quantifies the energization of the population in each pathway, the contributions from the electric field components using the following equation:

$$\Delta\epsilon_e = \int -ev_{||}E_{||}\mathrm{d}t + \int -e\boldsymbol{v}_\perp \cdot \boldsymbol{E}_\perp \mathrm{d}t \tag{4}$$

In the first pathway (accounting for 56% of the population), electrons are accelerated toward the DF in a single pass by the parallel electric field ($E_{||}$) along the magnetic field (Figures 6(a1)–(d1)). In this pathway, $E_{||}$ is the primary contributor to the total energy gain. In the second pathway (35% of the population), electrons are also drawn toward the midplane by $E_{||}$ but are subsequently trapped, executing a bouncing motion around the midplane (Figures 6(a2)–(d2)). The trapping mechanism is primarily provided by the parallel potential, since the magnetic mirror force is negligible due to their small magnetic moment. The third pathway (9% of the population) involves electrons that travel through the

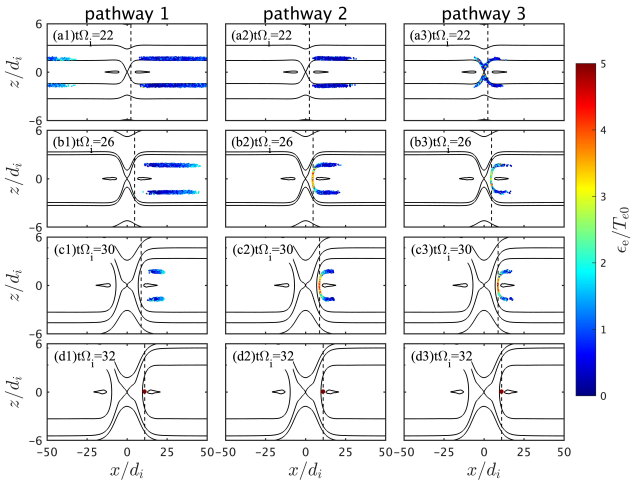

Figure 6. Spatial distributions of the retraced lower-energy population of energetic electrons at pitch angles near 0° and 180°($|\theta - 90°| > 60°$) at the DF involving in the three pathways at $t\Omega_i =$ 22, 26, 30, and 32, respectively. Those retraced electrons are denoted in black boxes in Figure 3(b2). The vertical dashed lines mark the location of the maximum of B along $z = 0$ in $x > 0$ domain at each time slot for reference. The colors represent the energies of electrons. The curves represent the magnetic field lines.

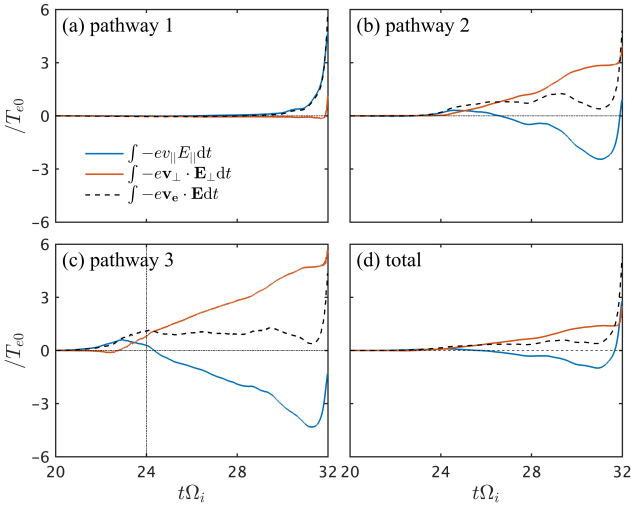

Figure 7. Time integration of the work done by electric field on (a)–(c) electrons involving in the three pathways and (d) the total population, averaging over electrons. The vertical dashed line in panel (c) marks the time when the electrons in the third pathway leaves the reconnection site.

reconnection site (Figure 6(a3)). They gain only modest amounts of energy from the reconnection electric field and are subsequently trapped by parallel potential. In the second and third pathways, the perpendicular electric field ($E_\perp$) primarily contributes the energy gain (Figures 7(b) and (c)). However, because the first pathway constitutes more than half of the population, the total averaged contribution from $E_{||}$ is comparable to that from $E_\perp$ (Figure 7(d)). Given the vital roles of parallel potential in both accelerating electrons toward the DF and providing the trapping mechanism, we conclude that the parallel potential dominates the formation of this population. These energization processes also explain why the energies of this population are close to the magnitude of the parallel potential. The electrons in the first pathway originating upstream are energized by the parallel potential and also

mildly accelerated by $E_{\perp}$, thus they arrive the DF with energies slightly exceeding the parallel potential. For electrons in the second and third pathways, their energies are limited by the parallel potential due to the confinement within the potential well.

4. Conclusions and Discussion

In summary, we investigate the formation of energetic electrons observed at the DF and FPR during magnetic reconnection by performing a two-dimensional PIC simulation. The energetic electrons in the FPR are predominantly concentrated at pitch angles near 90°, whereas those at the DF are observed at pitch angles near 0°, 90°, and 180°. Our results demonstrate that the 90° pitch-angle energetic electrons in the FPR and DF both undergo a two-stage acceleration process. They are initially energized near the X-line by the reconnection electric field and then transported downstream, where they experience further adiabatic acceleration. The energy gain in the first stage is critical in determining the final electron energy. Electrons arriving at the FPR travel through the reconnection site at a later time, when the reconnection electric field is stronger, granting them significantly greater energization (approximately 2.7 times that of electrons arriving at the DF in the first stage). The efficiency of the second-stage acceleration is determined by two factors: the relative change in magnetic field and the initial electron energy in this stage. Therefore, although electrons arriving at the DF experience a stronger magnetic field compression in the second stage, the insufficient preacceleration from the first stage limits the subsequent adiabatic acceleration. As a result, the electrons arriving at the FPR reach substantially higher energies than those arriving at the DF. Concurrently, two populations of energetic electrons with distinct energy ranges at pitch angles near 0° and 180° are identified at the DF. We demonstrate that the lower-energy population exhibits energies close to the magnitude of the parallel potential at the DF. The parallel potential dominates the formation of this population by accelerating the electrons toward the DF and providing the trapping mechanism. Meanwhile, the higher-energy population is energized via the Fermi mechanism through multiple reflections within contracting magnetic islands downstream.

The pioneering work of M. Hoshino et al. (2001) suggests that the nonadiabatic motion of electrons in the FPR plays an important role in electron energization. In their study, the employment of a relatively small simulation domain may limit the development of magnetic flux pileup, possibly leading to nonadiabatic motion of electrons around the midplane where the magnetic field remains moderate. The larger simulation domain employed in our work allows the FPR develop further, and the magnetic field around the midplane within the FPR intensifies to the order of the upstream magnetic field. Therefore, adiabatic motion dominates the acceleration process in the FPR in our results.

These simulation results provide a comprehensive interpretation for satellite observations of electron temperature anisotropy at the DF and FPR. Consistent with the observations in Y. V. Khotyaintsev et al. (2011), we reproduce the anisotropy of $T_{e\perp}/T_{e\parallel}>1$ in the FPR and the anisotropy of $T_{e\perp}/T_{e\parallel}<1$ at the DF in the later stage of reconnection (around $t\Omega_i = 40$ in our simulation). We propose that the temperature anisotropy in the FPR results from the effective perpendicular electron energization by the two-stage acceleration. The reversed anisotropy at the DF is attributed to the combined effect of (1) the increase of the electron parallel temperature resulting from both the enhanced parallel potential and the more sufficient Fermi acceleration, and (2) the reduction of the perpendicular flux due to particle loss at the DF.

Strong parallel potential can also form near the X-line during magnetic reconnection, particularly under low upstream β_e conditions (J. Egedal et al. 2013). J. Egedal et al. (2013) highlight its contribution to confining the electrons for a sufficiently long time for the energization at the reconnection site to become effective during antiparallel reconnection. We point out that both the 90° pitch-angle energetic population (the second-stage acceleration) and the lower-energy 0° and 180° population (electrons involved in the second and third pathways) at the DF share an analogous energization process, which underscores the importance of the parallel potential in producing energetic electrons during magnetic reconnection.

The earlier studies have investigated the outward-propagating energetic electrons in the outflow region that appear as part of the Hall current system (M. Øieroset et al. 2001; Q. Lu et al. 2010). In our results, we identify a significant population of inward-propagating energetic electrons in the outflow region (electrons in the first pathway shown in Figure 6), as well as a population executing bounce motion along the magnetic field (electrons in the second and third pathways shown in Figure 6). These populations can also contribute to the Hall current, which reveals a more complex picture of the Hall reconnection system.

Acknowledgments

This work is supported by the National Key Research and Development Program of China (No. 2022YFA1604600). The simulation dataset (the electromagnetic field data and particle data used to plot the figures in this work) can be downloaded from: 10.57760/sciencedb.30394.

ORCID iDs

Jia Nan https://orcid.org/0000-0001-8033-2336
Quanming Lu https://orcid.org/0000-0003-3041-2682
Kai Huang https://orcid.org/0000-0003-3630-309X
San Lu https://orcid.org/0000-0003-2248-5072
Rongsheng Wang https://orcid.org/0000-0002-9511-7660
Shihang Hu https://orcid.org/0009-0000-9423-5131

References

Angelopoulos, V., Baumjohann, W., Kennel, C. F., et al. 1992, JGR, 97, 4027
Angelopoulos, V., McFadden, J. P., Larson, D., et al. 2008, Sci, 321, 931
Angelopoulos, V., Runov, A., Zhou, X.-Z., et al. 2013, Sci, 341, 1478
Ashour-Abdalla, M., El-Alaoui, M., Goldstein, M. L., et al. 2011, NatPh, 7, 360
Birn, J., & Hesse, M. 2001, JGR, 106, 3737
Birn, J., Hesse, M., Nakamura, R., & Zaharia, S. 2013, JGRA, 118, 1960
Birn, J., Runov, A., & Hesse, M. 2014, JGRA, 119, 3604
Chang, C., Huang, K., Lu, Q., et al. 2021, JGRA, 126, e29290
Dai, L., Zhu, M., Ren, Y., et al. 2024, NatCo, 15, 639
Divin, A., Lapenta, G., Markidis, S., et al. 2012, JGRA, 117, A06217
Drake, J., Swisdak, M., Che, H., & Shay, M. 2006, Natur, 443, 553
Egedal, J., Daughton, W., Le, A., & Borg, A. L. 2015, PhPl, 22, 101208
Egedal, J., Le, A., & Daughton, W. 2013, PhPl, 20, 061201
Fu, H., Khotyaintsev, Y. V., Vaivads, A., Retinò, A., & André, M. 2013, NatPh, 9, 426
Fu, H. S., Khotyaintsev, Y. V., André, M., & Vaivads, A. 2011, GeoRL, 38, L16104
Fu, X. R., Lu, Q. M., & Wang, S. 2006, PhPl, 13, 012309
Fu, H., Xu, Y., Vaivads, A., & Khotyaintsev, Y. V. 2019, ApJL, 870, L22

Giovanelli, R. 1946, Natur, 158, 81
Hesse, M., & Birn, J. 1991, JGR, 96, 19417
Hoshino, M., Mukai, T., Terasawa, T., & Shinohara, I. 2001, JGR, 106, 25979
Hu, S., Lu, Q., Shu, Y., et al. 2025, ApJ, 986, 43
Huang, S., Fu, H., Yuan, Z., et al. 2015, JGRA, 120, 4496
Huang, K., Ling, W., Tang, H., et al. 2025a, PhPl, 32, 072901
Huang, K., Ling, W., Tang, H., et al. 2025b, GeoRL, 52, e2025GL117351
Huang, C., Lu, Q., & Wang, S. 2010, PhPl, 17, 072306
Huang, K., Lu, Q., Lu, S., Wang, R., & Wang, S. 2021, JGRA, 126, e29939
Huang, S., Vaivads, A., Khotyaintsev, Y. V., et al. 2012, GeoRL, 39, L11103
Huang, C., Wu, M., Lu, Q., Wang, R., & Wang, S. 2015, JGRA, 120, 1759
Khotyaintsev, Y. V., Cully, C., Vaivads, A., André, M., & Owen, C. 2011, PhRvL, 106, 165001
Lin, J., & Forbes, T. 2000, JGR, 105, 2375
Liu, C., Fu, H., Liu, Y., et al. 2020, JGRA, 125, e27777
Liu, C., Fu, H., Xu, Y., Cao, J., & Liu, W. 2017, GeoRL, 44, 6492
Liu, Y.-H., Hesse, M., Guo, F., et al. 2017, PhRvL, 118, 085101
Lu, S., Angelopoulos, V., & Fu, H. 2016, JGRA, 121, 9483
Lu, Q., Fu, H., Wang, R., & Lu, S. 2022, ChPhB, 31, 089401
Lu, Q., Huang, C., Xie, J., et al. 2010, JGRA, 115, A11208
Lu, S., Lu, Q., Lin, Y., et al. 2015, JGRA, 120, 6286
Lu, Q., Shu, Y., Chang, C., Lu, S., & Wang, R. 2025, SciBu, 70, 2766
Lu, Q., Wang, H., Huang, K., Wang, R., & Wang, S. 2018, PhPl, 25, 072126
McPherron, R. 1987, in Quantitative Modeling of Magnetosphere-Ionosphere Coupling Processes, ed. Y. Kamide & R. A. Wolf, 252
Mozer, F., Bale, S., & Phan, T. 2002, PhRvL, 89, 015002
Nagai, T., Shinohara, I., Fujimoto, M., et al. 2003, JGRA, 108, 1357
Nakamura, R., Baumjohann, W., Klecker, B., et al. 2002, GeoRL, 29, 3
Nan, J., Huang, K., Lu, Q., et al. 2022, JGRA, 127, e29996
Nishida, A., & Akasofu, S.-I. 1979, Geomagnetic Diagnosis of the Magnetosphere (AIP)
Øieroset, M., Lin, R., Phan, T., Larson, D., & Bale, S. 2002, PhRvL, 89, 195001
Øieroset, M., Phan, T., Fujimoto, M., Lin, R., & Lepping, R. 2001, Natur, 412, 414
Oka, M., Birn, J., Egedal, J., et al. 2023, SSRv, 219, 75
Pritchett, P. 2001, JGR, 106, 3783
Runov, A., Angelopoulos, V., Sitnov, M., et al. 2009, GeoRL, 36, L14106
Shu, Y., Lu, S., Lu, Q., Ding, W., & Wang, S. 2021, JGRA, 126, e29712
Sitnov, M., Swisdak, M., & Divin, A. 2009, JGRA, 114, A04202
Sweet, P. 1958, IAUS, 6, 123
Tsuneta, S., Hara, H., Shimizu, T., et al. 1992, PASJ, 44, L63
Wang, R., Lu, Q., Du, A., & Wang, S. 2010a, PhRvL, 104, 175003
Wang, R., Lu, Q., Huang, C., & Wang, S. 2010b, JGRA, 115, A01209
Wang, S., Lu, S., Lu, Q., et al. 2024, SciA, 10, eado4639
Wang, R., Yu, X., Wang, Y., Lu, Q., & Lu, S. 2023, ApJ, 947, 78
Wu, M., Huang, C., Lu, Q., et al. 2015, JGRA, 120, 6320
Wu, M., Lu, Q., Volwerk, M., et al. 2013, JGRA, 118, 4804
Xing, X., Liu, C., Cao, J., Liu, Y., & Zhao, B. 2024, ApJ, 972, 10
Xu, Y., Fu, H., Liu, C., & Wang, T. 2018, ApJ, 853, 11
Yamada, M., Kulsrud, R., & Ji, H. 2010, RvMP, 82, 603
Yang, F., Lu, Q., Zhang, Q., et al. 2025, GeoRL, 52, e2024GL114151
Yu, Y., Fu, H., Wang, Z., Fu, W., & Cao, J. 2023, GeoRL, 50, e2023GL104938
Zhang, T., Lu, Q., Baumjohann, W., et al. 2012, Sci, 336, 567
Zhang, H., Pu, Z., Cao, X., et al. 2007, GeoRL, 34, L03104
Zhou, M., Deng, X., Ashour-Abdalla, M., et al. 2013, JGRA, 118, 674